JOURNAL OF SYNCHROTRON RADIATION
ISSN 1600-5775

Comparison of helical scan and standard rotation methods in single-crystal X-ray data collection strategies

Ivan Polsinelli,[a,b]‡ Martin Savko,[a] Cecile Rouanet-Mehouas,[c] Lidia Ciccone,[a,c] Susanna Nencetti,[b] Elisabetta Orlandini,[b] Enrico A. Stura[a,c] and William Shepard[a]*

[a]Synchrotron SOLEIL, L'Orme des Merisiers, Saint-Aubin, BP 48, 91192 Gif-sur-Yvette, France, [b]Dipartimento di Farmacia, Università di Pisa, Via Bonanno 6, 56126 Pisa, Italy, and [c]CEA, iBiTec-S, Service d'Ingénierie Moléculaire des Protéines (SIMOPRO), F-91191 Gif-sur-Yvette, France. *Correspondence e-mail: william.shepard@synchrotron-soleil.fr

Received 1 August 2016
Accepted 18 November 2016

Edited by E. F. Garman, University of Oxford, England

‡ Current address: Free University of Bozen-Bolzano, Faculty of Science and Technology, Piazza Universitá 5, 39100 Bolzano (BZ), Italy.

Keywords: helical scans; radiation damage; bromophenyl ligands; micro-focus; PROXIMA 2A.

Supporting information: this article has supporting information at journals.iucr.org/s

X-ray radiation in macromolecular crystallography can chemically alter the biological material and deteriorate the integrity of the crystal lattice with concomitant loss of resolution. Typical alterations include decarboxylation of glutamic and aspartic residues, breaking of disulfide bonds and the reduction of metal centres. Helical scans add a small translation to the crystal in the rotation method, so that for every image the crystal is shifted to expose a fresh part. On beamline PROXIMA 2A at Synchrotron SOLEIL, this procedure has been tested with various parameters in an attempt to understand how to mitigate the effects of radiation damage. Here, the strategies used and the crystallographic metrics for various scenarios are reported. Among these, the loss of bromine from bromophenyl moieties appears to be a useful monitor of radiation damage as the carbon–bromine bond is very sensitive to X-ray irradiation. Two cases are focused on where helical scans are shown to be superior in obtaining meaningful data compared with conventional methods. In one case the initial resolution of the crystal is extended over time, and in the second case the anomalous signal is preserved to provide greater effective multiplicity and easier phasing.

1. Introduction

Synchrotron radiation is currently the dominant X-ray source for collecting X-ray diffraction data from single crystals of biological macromolecules. However, exposure to the intense X-ray beams causes severe damage to the crystal, altering its chemical nature at specific sites, especially for the heavier atoms that may reside at biochemically active sites, and distorting the crystalline lattice. These effects may even prevent the collection of a complete data set, compromising the quality of the final electron density map. Any radiation damage inflicted during data collection in macromolecular crystallography (MX) can result in severe degradation of data quality and the appearance of artefacts, which adversely affect the interpretation of the electron density. The symptoms of radiation damage are varied and are not always directly observable. The most common are the reduction in reflection intensities starting from the highest resolution shells, the decrease in the internal consistency of the data, the increase in unit cell volume, colour changes and visible differences in the crystal (Gerstel *et al.*, 2015; Garman, 2010). Structural damage can affect covalent bonds: disulfide bridges may elongate and then break, glutamate and aspartate residues may become decarboxylated and carbon–sulfur bonds may break in methionine residues. Metal centres are also reduced by relatively

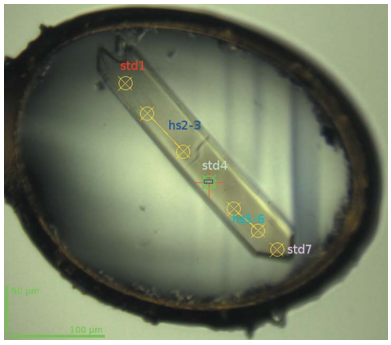

low X-ray doses (Gerstel *et al.*, 2015; Weik *et al.*, 2000, 2002; Burmeister, 2000; Ravelli & McSweeney, 2000). All these changes could prevent the correct structural interpretation to understand the underlying biology.

Therefore, radiation damage in MX is an increasingly important and limiting problem. In multi-wavelength anomalous diffraction (MAD) experiments, data collected for the second and third X-ray wavelength are often much weaker, which prevents the effective measurement of the anomalous scattering from the sub-structure, leading to a type of non-isomorphism that results in the failure of the phasing experiment. In more extreme cases, radiation-sensitive crystals degrade before the data reach completion, so that several crystals need to be merged together to give a complete data set (Liu *et al.*, 2012, 2013; Garman, 2010).

The amount of damage caused by X-ray radiation is correlated to the absorbed dose. Recently developed software, *RADDOSE-3D* (Zeldin, Gerstel *et al.*, 2013), allows users to simulate the progression of the absorbed energy given different experimental parameters to generate a spatial map of the expected dose profile over the crystal. Programs such as *EDNA* (Incardona *et al.*, 2009) and *BEST* (Bourenkov & Popov, 2010) coupled with the user interface *MXCuBE* (Gabadinho *et al.*, 2010) exploit the initial X-ray diffraction test images to calculate optimal parameters to allow collection of a complete data set before the crystal is too severely damaged by radiation.

On micro-focus beamlines the crystal can be much larger than the beam and rotation data collected at a single position exploit only a fraction of the crystal volume. To spread the overall dose over a greater volume of the crystal, a small translation can be applied during the rotation, a strategy referred to as helical scan (Flot *et al.*, 2010). Similar strategies, vector scan (Hilgart *et al.*, 2011) and line scan (Song *et al.*, 2007), also continuously expose a fresh portion of the crystal to X-rays with the potential of reducing the effects of radiation damage on the collected data. Depending on the size and geometry, these strategies permit the crystallographer to improve the completeness and multiplicity obtained from each crystal.

Helical scans require beam-positional stability and high-precision mechanics to achieve a smooth movement while scanning the length of the crystal (Shayduk & Braun, 2008). Any mechanical roughness, wobble or twist in the goniometer translation stages would cause minor crystal misalignments that could have dramatic effects on the integration of the images affecting the final data quality, if not properly corrected by the data processing software. Such crystal misalignments would deteriorate data in the same manner as vibrations induced by pulses from a cryostream jet on unstable mounting loops (Alkire *et al.*, 2013). Crystalline inhomogeneity, such as cracks, splits, growth and lattice defects, will affect the diffraction pattern and complicate scaling. Even a visually flawless crystal may have a certain amount of intra-crystal variability (Bowler *et al.*, 2010; Bowler & Bowler, 2014; Pozharski, 2012). Such variability that may originate during crystal growth or from inhomogeneous desiccation during crystal handling or flash-cooling will be shown by small variations in the unit-cell parameters and in the diffracted intensities. Fearing that this technique might complicate matters for crystallographic calculations without providing significant gains, many crystallographers shun helical scans, a method implemented at many MX beamlines.

We present an excerpt of a comparative study of helical *versus* standard MX data collections carried out using micro-focused X-rays (FWHM 10 µm × 5 µm) on the beamline PROXIMA 2A at Synchrotron SOLEIL. The experiments devised for this study attempt to compare single-crystal X-ray diffraction data collected under similar conditions using the usual metrics prominent in MX. The selected cases are examples that aim to illustrate the benefits rather than the limitations of helical scans.

2. Material and methods

2.1. Sample preparation

The samples used in these comparative MX experiments were crystals of human transthyretin (TTR), human matrix metalloproteinase 12 (MMP-12) and selenomethionine substituted maltose operon periplasmic protein (MalM). The crystals of TTR and MMP-12 were prepared using previously published protocols (Vera *et al.*, 2013; Ciccone *et al.*, 2015). The crystal structure determination of MalM (Gilson *et al.*, 1986) is an ongoing research project, and the protein preparation and crystallization conditions will be described in a future publication after its crystal structure is resolved and analysed (A. Haouz, private communication).

2.2. Beamline parameters

Single-crystal X-ray diffraction data were collected on the beamline PROXIMA 2A at Synchrotron SOLEIL (Duran *et al.*, 2013), which is tunable in the 6–15 keV range and focuses a maximum flux in excess of 10^{12} photons s^{-1} into a Gaussian-shaped spot size of 10 µm × 5 µm (H × V, FWHM). To reduce the background scatter, the X-ray beam edges are trimmed with a 50 µm pinhole and guard collimator just upstream of the sample. The flux is monitored continuously on the beamline using X-ray beam position monitors (Morse *et al.*, 2007; Alkire *et al.*, 2000), which were calibrated to the flux at the sample position using a calibrated silicon photodiode (AXUV 100, 10 mm × 10 mm active area, 52 µm-thick silicon; Opti Diode Corporation). The instrumentation of the experimental station includes a high-performance goniometer (Micro-Diffractometer MD2, MAATEL-ARINAX), comprising a high-precision air-bearing rotation axis and sub-micrometre resolution centring table with two translations, and an ADSC Q315 area detector. Most of the X-ray diffraction data were collected at λ = 0.98012 Å (12.65 keV), which is the standard X-ray wavelength of the beamline, except for those crystals containing bromine or selenium as anomalous scatterers. X-ray diffraction data on crystals containing brominated ligands were collected at λ = 0.91841 Å (13.5 keV), just on the high-energy side of the bromine absorption *K*-edge (λ =

0.9202 Å or 13.474 keV), and X-ray diffraction data for the selenomethionated crystals were collected at the peak of the fluorescence energy scan at λ = 0.97896 Å (12.665 keV). All data were collected from cryo-cooled crystals kept at 100 K using a CryoStream 700 (Oxford Cryosystems).

2.3. Crystal centring and data collection methods

In our initial tests, data were collected by the standard rotation method about a fixed point around an axis perpendicular to the X-ray beam (standard method: STD). Then, starting from an adjacent point at least 20 µm away, the crystal was translated along its length between each image during the rotation (helical scan method: HS). The HS method used here is a set of points along the length of the crystal, and resembles that used on beamline ID23-2 at the ESRF (Flot *et al.*, 2010). A variety of combinations of STD and HS data collections were thus used for comparison depending upon the length of the crystal. In general, for shorter crystals, a standard scan was collected towards one end of the crystal, followed by a helical scan, and then another standard scan towards the opposite end of the crystal (Fig. 1*a*). If the length of the crystal permitted, three standard scans were alternated with two helical scans (Fig. 1*b*).

In many preliminary experiments, due to optical effects induced by the surrounding cryoprotectant, the needle-like crystals were difficult to centre visually and several were not aligned in the X-ray beam. This problem is quite common and stems from positional aberrations that shift the crystal image away from its true centre. The consequences were poor statistics for those data wedges where only a fraction of the crystal was coincident with the X-ray beam. To improve centring, we adjusted the protocol to include a positional low-dose scan (1–3% transmission) in which a series of X-ray diffraction images were collected while the crystal was translated perpendicularly to both the X-ray beam and the rotation axis. The final strategy consisted of low-dose X-ray centring to choose at which point to collect the STD data and determine the two extremes for the HS data collection. An additional set of four images were collected at moderate dose (5–10% transmission) at a remote point on the crystal, for use in the data collection optimization strategy implemented by *EDNA* and *BEST* (Incardona *et al.*, 2009; Leal *et al.*, 2011; Bourenkov & Popov, 2010). The data collection parameters suggested by these programmes were applied to both the STD and HS data collection. For single-wavelength anomalous diiffraction (SAD) data, higher multiplicity was prioritized in order to aid the phasing steps in structure determination.

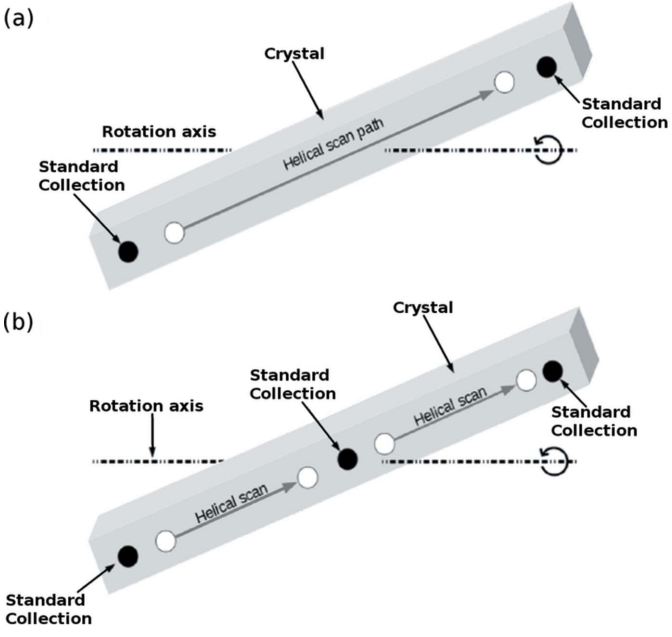

Figure 1
Schematic diagrams describing the data acquisition strategies used for helical (HS) and standard (STD) scans. (*a*) Standard data collections were performed at either end of the crystal with a helical scan in between. (*b*) For longer crystals, three standard data collections were carried out in the centre and at either end with two helical scans in between the middle point and either extreme.

2.4. Data processing

All diffraction images were indexed, integrated and scaled with *XDS* (Kabsch, 2010*a*) *via* the *XDSME* script (https://github.com/legrandp/xdsme). Plots of the MX metrics table in *XDS* were generated and for comparison were drawn with a Python script employing *matplotlib* modules. The CCP4i interface was used to perform molecular replacement (Vagin & Teplyakov, 2010), and rigid body and restrained refinement (Murshudov *et al.*, 2011). Model phases and DANO columns were appended to the MTZ files using *SFALL* and *CAD* from the *CCP4* package (Winn *et al.*, 2011). The starting model for molecular replacement calculations for the TTR crystals were from the PDB code 3esp (Johnson *et al.*, 2009). *PHENIX.AUTOBUILD* (Adams *et al.*, 2010; Terwilliger *et al.*, 2008) was used to trace automatically and refine crystal structures of TTR co-crystallized with a low-affinity chlorine-containing ligand. SAD phasing on the TTR crystals complexed with brominated ligand (Fig. 3) was performed using the *HKL2MAP* interface (Pape & Schneider, 2004) to *SHELXC/D/E* (Sheldrick, 2002, 2008; Schneider & Sheldrick, 2002). Visual inspection of the maps and fitting of the electron density was performed using *COOT* (Emsley *et al.*, 2010). The figures were made using *COOT* and *PyMOL* v.1.3 (http://www.pymol.org; Schrödinger).

3. Results

Although a large number of crystals were used in this comparative study, for reasons of brevity, only three or four representative cases for each system are reported (see also the supporting information).

Images of all data sets were closely inspected to filter out flaws (*e.g.* split Bragg spots), which would render comparison between STD and HS strategies meaningless. Processing of the images was launched with identical parameters and then these parameters were allowed to refine independently to optimize the integration of the experimental X-ray intensities.

Table 1
Crystallographic statistics for TTR.

Estimated crystal dimensions: 20 µm × 20 µm × 380 µm. Data collection parameters: X-ray wavelength, 0.9801 Å; 0.5 s exposure per image; 180 images; 0.5° oscillation range; total angular sweep, 90°. Values in parentheses are for the outer resolution shell.

Data collection mode (acronym)	Standard (std1)	Helical (hs2-3)	Standard (std4)	Helical (hs5-6)†	Standard (std7)
Space group	$P2_12_12$	$P2_12_12$	$P2_12_12$	$P2_12_12$	$P2_12_12$
Unit-cell parameters: *a, b, c* (Å)	43.22, 85.03, 63.39	43.40, 85.57, 63.39	43.22, 85.09, 63.46	43.33, 85.04, 63.26	43.30, 84.66, 63.22
Wavelength (Å)	0.9801	0.9801	0.9801	0.9801	0.9801
X-ray flux (photons s^{-1})	3.2×10^{11}	3.2×10^{11}	3.2×10^{11}	3.2×10^{11}	3.2×10^{11}
Helical scan pace	–	110 µm / 90°	–	120 µm / 90°	–
Resolution range (outer shell) (Å)	38.8–1.80 (1.90–1.80)	38.7–1.80 (1.90–1.80)	38.7–1.80 (1.90–1.80)	38.7–1.80 (1.90–1.80)	38.7–1.80 (1.91–1.80)
Total No. reflections	77693 (11821)	79145 (11680)	77991 (11707)	77625 (11527)	76013 (11747)
No. unique reflections	22144 (3381)	22437 (3404)	22202 (3360)	19675 (3107)	21991 (3366)
Completeness	98.5% (95.0%)	98.6% (94.4%)	98.4% (93.8%)	87.3% (86.7%)	98.4% (94.8%)
Multiplicity	3.51 (3.50)	3.53 (3.43)	3.51 (3.48)	3.95 (3.71)	3.46 (3.49)
$\langle I/\sigma_I \rangle$	4.12 (0.38)	8.63 (1.21)	5.34 (0.44)	11.67 (2.02)	3.82 (0.44)
R_{meas}	31.4% (477.7%)	11.8% (122.1%)	24.1% (470.6%)	8.7% (74.4%)	38.0% (513.9%)
$CC_{1/2}$	98.9% (4.3%)	99.6% (48.5%)	99.3% (8.3%)	99.8% (63.9%)	97.3% (15.1%)
CC_{ano}	−2% (4%)	−9% (−10%)	−8% (1%)	−4% (−1%)	−11% (−6%)
σ_{ano}	0.696 (0.567)	0.731 (0.676)	0.698 (0.567)	0.761 (0.739)	0.648 (0.506)
RADDOSE-3D results					
Average diffraction weighted dose (MGy)	37.43	8.70	37.43	8.19	37.43
Elastic yield (photons)	1.1×10^{10}	1.1×10^{10}	1.1×10^{10}	1.1×10^{10}	1.1×10^{10}
Diffraction efficiency (photons MGy^{-1})	3.0×10^{8}	1.3×10^{9}	3.0×10^{8}	1.4×10^{9}	3.0×10^{8}
Average dose (exposed region) (MGy)	21.4	5.5	21.4	5.1	21.5
Maximum dose (MGy)	203.0	19.2	203.0	17.6	203.0
Dose contrast	4.3	1.8	4.3	1.7	4.3
Used volume, fractional	7.8%	30.4%	7.8%	32.5%	7.8%
Used volume, absolute (μm^3)	11856	46208	11856	49400	11856
PHENIX.AUTOBUILD results					
Rwork / Rfree	0.2322 / 0.2860	0.1982 / 0.2198	0.2160 / 0.2605	0.1902/ 0.2190	0.2643 / 0.3106
Natoms	1872	1924	1866	1900	1868

† The data set hs5-6 was collected over a different segment of reciprocal space.

For the representative cases, we have calculated the doses deposited on the crystals using *RADDOSE-3D* (Zeldin, Gerstel *et al.*, 2013), which determines several dose metrics using dimensions of the crystals as estimated from the snapshots and X-ray centring scans.

3.1. Human transthyretin crystals

TTR crystallizes in $P2_12_12$ with unit cell constants a = 43.5 Å, b = 85.9 Å, c = 64.1 Å. Snapshots of the TTR crystals are shown in Figure S1 of the supporting information. The crystals used in this study were 100–400 µm long in one dimension, but typically less than 50 µm thick in the other two. Crystallographic data for TTR crystals are presented in Table 1. In the first case, the crystal was long and thin (20 µm × 20 µm × 380 µm). Three STD data sets (std1, std4 and std7) and two HS data sets (hs2-3 and hs5-6) were recorded. The flux of the X-rays was 3.2×10^{11} photons s^{-1} at 12.65 keV, which corresponds to an average diffraction weighted dose for the exposed region of 37.43 MGy for STD data, and 8.19 MGy (hs2-3) and 8.70 MGy (hs5-6) for HS data as calculated by *RADDOSE-3D*. Both HS data sets gave superior quality indicators than the three STD data sets, which were collected before and after each HS data set (see Fig. S1). Since map quality is the ultimate metric, close attention has been paid to the refined $2F_o - F_c$ maps. Although these may appear identical at first glance (because the maps are dominated by the phases calculated from the model coordinates), upon closer inspection the maps obtained from the HS data show greater detail than those from STD data (Figs. 2 and S2). The improvement might be due to the stronger diffraction signal in the higher-resolution shells (1.8 Å) of the HS data compared with the STD data.

3.2. TTR crystals containing brominated ligands

Certain organohalogen compounds, including many brominated compounds, bind strongly to human TTR as shown by *in vitro* assays (Meerts *et al.*, 2000). Since the bromine is easily lost from various ligands as a result of X-ray irradiation (Ennifar *et al.*, 2002), preservation of its anomalous signal was adopted as an internal measure of reduced radiation damage with different data collection strategies. C—Br bonds are particularly sensitive to X-rays at energies at and just above the Br *K*-edge (13.4737 keV). Two crystals were compared, both diffracting to 1.4 Å; for the first crystal with dimensions of 45 µm × 45 µm × 175 µm (Fig. 3) the metrics for the HS data, which had an overall better resolution, were found to be significantly better than for the STD data. The anomalous signal from the bromine atoms extended to higher

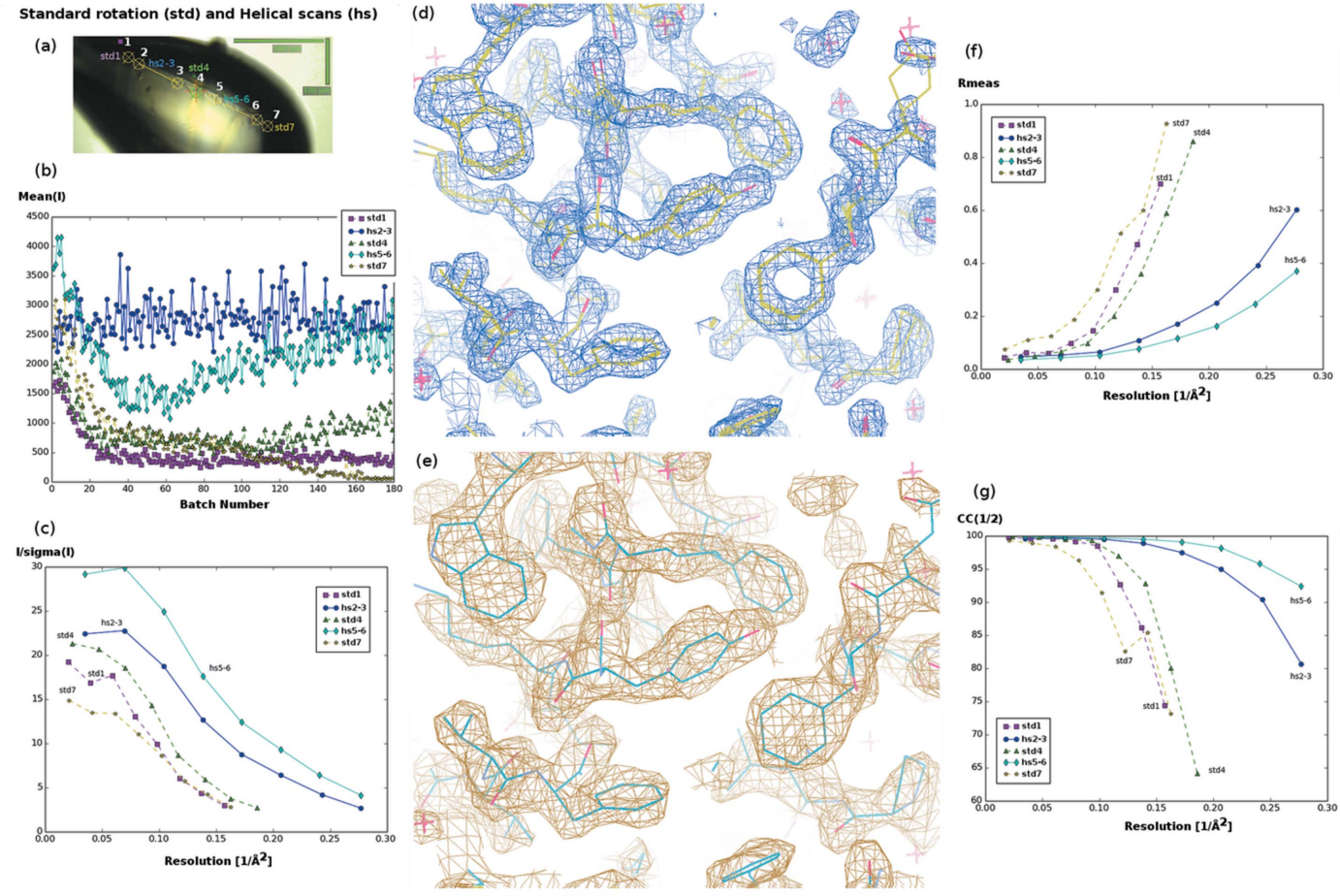

Figure 2
Comparison of STD and HS data collection methods with a TTR crystal complexed with a chlorinated ligand. (*a*) Snapshot of the TTR crystal with the positions 1, 4 and 7 of the STD data collections (std1, std4 and std7), and traces of the HS scans between positions 2 and 3 (hs2-3) and between positions 5 and 6 (hs5-6) marked. (*b*) Plots of the *B*-factor as a function of batch number, which show less decay in the HS data collections (hs2-3 and hs5-6) compared with STD data collections (std1, std4 and std7). For std7, which was collected at 100% flux, the scaling fails after frame 110. (*c*) Plots of $\langle I/\sigma_I \rangle$ *versus* resolution. (*d*, *e*) Automatically built and traced electron density contoured at 1.5 standard deviations for the hs2-3 (top) and std1 (bottom) data sets, respectively. The detail in the hs2-3 map is clearly superior to the std1 map. (*f*, *g*) Plots of $R_{\rm meas}$ and $CC_{1/2}$ *versus* resolution.

resolution for both HS data sets, allowing the phases to be easily calculated (estimated ⟨FOM⟩ = 0.682, pseudo-free CC = 74.08% from *SHELXE*), while phasing with the STD data set failed despite several attempts with various input parameters (best estimated ⟨FOM⟩ = 0.435). The phased map for the HS data set is very clear showing distinct electron density for virtually all of the main-chain and side-chain atoms, whereas that for the STD data does not allow even the main chain to be traced (Fig. 3). The anomalous peaks for the bromine atoms were higher in the phased anomalous Fourier maps calculated from the HS data by at least 50% (Table 2; Fig. S3). For the last crystal, the HS data were comparable with the STD data (Fig. S1, column 4). The anomalous peaks are very strong (over 40 standard deviations above the mean) and comparable between the std1 and the hs2-3 data, while the peaks for the hs4-5 data are slightly weaker. In this case, the HS strategy did not yield better data compared with STD protocol. With a particularly thick sample (crystal dimensions of 100 µm × 100 µm × 350 µm; Fig. S1, column 4), much larger than the fine vertical focus of the beam on PROXIMA 2A (5 µm, FWHM), only a small improvement was expected. The weaker hs4-5 data are explained by the reduced thickness of the crystal over the scan length, even if the overall volume over the whole length of the scan was comparable. In addition, the average diffraction weighted dose for the exposed region is only 20.5 MGy for the STD data collection and 11.7 MGy and 7.8 MGy for the two HS data sets, all well below the Garman limit of 30 MGy (Owen *et al.*, 2006). In this scenario, the crystal is thicker and the beam is small and finely focused, a relatively fresh portion of crystal becomes exposed after each rotation step even during STD data collection. Unsurprisingly, the HS data collection did not provide any improvement.

The length of the translation during the HS data collection was varied to assess the importance of this parameter. Although significant differences were expected between the two HS data sets with different scan lengths (43 µm and 89 µm for the first crystal, and 52 µm and 180 µm for the second), the longer scan provided data that were only marginally better: it gave comparable crystallographic metrics and, judging from the height of the anomalous peaks, the statistics for the two data sets are largely equivalent (Table 2 and Fig. S1, column 3).

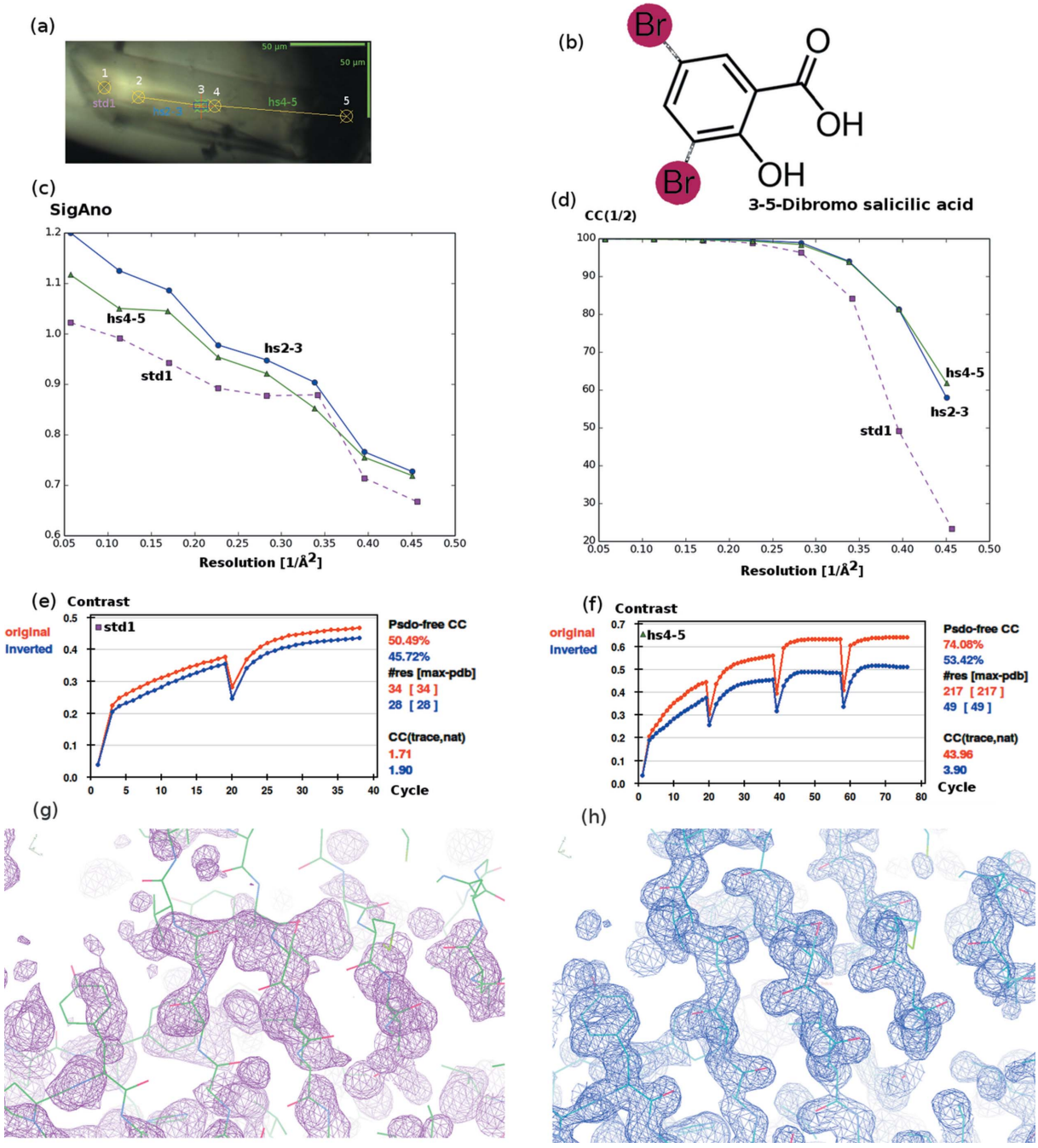

Figure 3
Bromine phasing experiments with 3,5-dibromosalicilic acid using STD and HS scans. (*a*) Snapshot of the crystal with the position 1 of the STD and traces of the HS scans between position 2 and 3 and between position 4 and 5. (*b*) Chemical structure of 3,5-dibromosalicilic acid showing the weak bond (dotted grey) between the bromine atoms (brown), the phenyl ring to which they are covalently bound. These bonds are susceptible to X-rays. (*c*, *d*) Plots of σ_{ano} and $CC_{1/2}$, respectively, showing better statistics for the HS scans. (*e*, *f*) Contrast *versus* cycle plots from *SHELXE* phasing (Sheldrick, 2002) displayed in *HKL2MAP* (Pape & Schneider, 2004) for the STD data (left) and the HS data (right), showing successful phasing for the HS data but failing for the STD data. (*g*–*h*) Untraced phased maps contoured at 1.5 standard deviations for STD (*g*) and HS (*h*). Only the HS map is easily traceable (model placed into electron density manually). The separation between the identified bromine atoms in the STD data is correct. However, using these atoms, to superimpose the TTR model into the density, shows the inferior quality of the STD data phasing with numerous breaks in the β strands and false connections.

3.3. Human matrix metalloproteinase 12

MMP-12 contains two zinc and three calcium binding atoms, and crystallizes in $P2_12_12$ with unit cell constants a = 68.4 Å, b = 62.5 Å, c = 37.1 Å. The peptidase activity is located at one zinc site, to which inhibitors bind. The crystals grow as long (>100 µm) plates or large thick prisms, which diffract well beyond 1.7 Å resolution. Several X-ray diffraction data sets were collected from these crystals for this comparative study, and, as these crystals are fairly long, often more than one set of

Table 2
Crystallographic statistics for TTR complexed with a brominated ligand.

Data set designation: TTR-Br_1; estimated crystal dimensions, 45 μm × 45 μm × 175 μm; X-ray wavelength, 0.91840 Å; 0.5 s exposure per image; 180 images; 0.5° oscillation range; total angular sweep, 90°. Values in parentheses are for the outer resolution shell.

Data collection mode (acronym)	Standard (std1)	Helical (hs2-3)	Helical (hs4-5)
Space group	$P2_12_12$	$P2_12_12$	$P2_12_12$
Unit-cell parameters: *a, b, c* (Å)	43.43, 85.95, 63.67	43.41, 86.01, 63.61	43.34, 85.90, 63.52
Wavelength (Å)	0.91840	0.91840	0.91840
X-ray flux (photons s^{-1})	2.5×10^{11}	2.5×10^{11}	2.5×10^{11}
Helical scan pace	–	43 μm / 90°	89 μm / 90°
Resolution range (outer shell) (Å)	43.0–1.40 (1.48–1.40)	43.0–1.40 (1.48–1.40)	43.0–1.40 (1.48–1.40)
Total No. reflections	333484 (50830)	335868 (51814)	332801 (51550)
No. unique reflections	89795 (14279)	89877 (14366)	89283 (14298)
Completeness	98.9% (97.2%)	99.3% (98.4%)	99.3% (98.4%)
Multiplicity	3.71 (3.56)	3.74 (3.61)	3.73 (3.61)
$\langle I/\sigma_I \rangle$	8.03 (0.41)	11.75 (0.85)	9.92 (0.95)
R_{meas}	12.7% (356.2%)	8.1% (182.8%)	10.1% (166.4%)
$CC_{1/2}$	99.8% (8.5%)	99.9% (27.2%)	99.8% (32.1%)
CC_{ano}	9% (0%)	11% (1%)	10% (−1%)
σ_{ano}	0.797 (0.601)	0.874 (0.681)	0.844 (0.659)
RADDOSE-3D results			
Average diffraction weighted dose (MGy)	20.5	11.7	7.8
Elastic yield	2.0×10^{10}	2.0×10^{10}	2.0×10^{10}
Diffraction efficiency (photons MGy^{-1})	9.9×10^{8}	1.7×10^{9}	2.6×10^{9}
Average dose (exposed region) (MGy)	10.0	6.1	4.2
Maximum dose (MGy)	168.6	40.8	19.7
Dose contrast	7.7	2.7	2.0
Used volume, fractional	13.6%	22.2%	31.9%
Used volume, absolute (m^3)	48195	78671	113046
Phased anomalous Fourier results			
Peak 1 (r.m.s.)	19.0	29.3	27.5
Peak 2 (r.m.s.)	13.9	20.2	22.6
SHELXE phasing results (both hands)			
Peak 1 (r.m.s.)	50.54 / 50.83	58.93 / 57.59	48.19 / 44.62
Peak 2 (r.m.s.)	36.34 / 33.39	51.72 / 47.53	43.57 / 50.22
Peak 3 (r.m.s.)	9.29 / 11.27	9.09 / 4.59	– / –
Estimated ⟨FOM⟩	0.435 / 0.398	0.441 / 0.613	0.477 / 0.682
Pseudo-free CC	50.49% / 45.72%	49.68% / 67.55%	53.42% / 74.08%

STD and HS data could be collected (Table 3, Fig. S4) from a single-crystal. For these crystals, it was not intended to exploit the anomalous scattering effects of the zinc sites, since the crystal structure is already well known. Thus the X-ray diffraction data were collected at the nominal energy of the beamline, 12.65 keV, which is far from the zinc *K*-edge (9.6586 keV). Consequently, the data collection strategies employed yielded rather low multiplicity (∼2.7 or ∼1.35 Bijvoet pairs), which were too low to directly phase from the relatively weak anomalous signal of the zinc atoms (∼2.5 electrons). However, the zinc atoms do appear in phased anomalous Fourier maps. Although this particular data set and its corresponding structure have not been deposited in the PDB, of the HS data collected on MMP-12 crystal structures, three have already been deposited (PDB codes 5d2b, 5d3c and 5czm).

The dimensions of the crystal described here were estimated to be 45 μm × 45 μm × 280 μm, from which five data sets were collected: three standard data collections at different X-ray beam fluxes, interpolated with two helical scans (Fig. S4, column 3). The results, given in Table 3, show that the average diffraction weighted dose varies from 1.25 to 24.29 MGy, with data quality comparable between the STD and HS data. The peaks from the phased anomalous Fourier maps confirm this (Fig. S5), and the peak heights are similar between the data sets (Table 3). Furthermore, increasing the incident flux (and consequently the dose rate) had little effect on the anomalous peak heights at the zinc sites. While this may seem counter-intuitive, it actually reflects certain physical realities. Zinc ions are resistant to X-ray radiation damage since they cannot be easily reduced (or oxidized) and in MMP-12 they are bound by at least three protein side-chains. This stable configuration is unlike one where a weak C—Br bond can be easily cleaved to yield a bromide ion that can diffuse away. Furthermore, the relative thickness of 45 μm of the MMP-12 crystal (compared with only 20 μm for the TTR crystal without the brominated ligand; see Fig. S1, column 1) coupled to the fine vertical focus (5 μm FWHM), effectively spreads out the dose over a greater volume in the directions perpendicular to the rotation axis, even for the STD data collections. Thus a factor of less than two between STD and HS data collection volumes has a minor effect. The differences in crystal thickness and X-ray sensi-

Table 3
Crystallographic statistics for MMP-12.

Crystal name: MMP12K_COOH_xtal9; dimensions: 45 μm × 45 μm × 280 μm; X-ray wavelength: 0.9801 Å; exposure time 0.5 s; oscillation range per image 0.5°; total angular sweep, 129°.

Data collection mode (acronym)	Standard (std1)	Helical (hs2-3)	Standard (std4)	Helical (hs5-6)	Standard (std7)
Space group	$P2_12_12$	$P2_12_12$	$P2_12_12$	$P2_12_12$	$P2_12_12$
Unit-cell parameters: *a, b, c* (Å)	68.924, 62.249, 37.723	68.554, 62.572, 37.294	68.604, 62.782, 37.231	68.820, 62.432, 37.539	43.30, 84.66, 63.22
Wavelength (Å)	0.9801	0.9801	0.9801	0.9801	0.9801
X-ray flux (photons s^{-1})	8.0×10^{10}	8.0×10^{10}	2.5×10^{11}	2.5×10^{11}	8.0×10^{11}
Helical scan pace	–	58 μm / 129°	–	37 μm / 129°	–
Resolution range (outer shell) (Å)	46.20–1.69 (1.79–1.69)	46.20–1.69 (1.79–1.69)	46.20–1.68 (1.78–1.68)	46.20–1.69 (1.79–1.69)	46.20–1.69 (1.79–1.69)
Total No. reflections	93646 (14645)	91809 (14167)	90960 (13956)	90575 (13937)	91203 (13631)
No. unique reflections	34476 (5494)	34141 (5408)	34262 (5376)	34065 (5405)	33773 (5155)
Completeness	98.5% (96.8%)	98.0% (95.9%)	97.3% (94.6%)	97.2% (95.2%)	96.2% (90.3%)
Multiplicity	2.72 (2.67)	2.69 (2.62)	2.65 (2.60)	2.66 (2.58)	2.70 (2.64)
$\langle I/\sigma_I \rangle$	6.66 (0.93)	6.99 (0.76)	5.71 (1.02)	5.89 (0.85)	6.07 (0.76)
R_{meas}	16.5% (157.3%)	16.0% (237.1%)	15.0% (146.9%)	16.3% (166.4%)	17.8% (192.9%)
$CC_{1/2}$	99.4% (37.1%)	99.4% (30.9%)	99.1% (44.1%)	99.2% (46.1%)	99.2% (63.5%)
CC_{ano}	9% (4%)	11% (3%)	27% (8%)	26% (3%)	4% (2%)
σ_{ano}	0.834 (0.676)	0.828 (0.627)	0.891 (0.640)	0.913 (0.642)	0.788 (0.707)
RADDOSE-3D results					
Average diffraction weighted dose (MGy)	2.43	1.25	7.59	4.79	24.29
Elastic yield	3.06×10^9	3.06×10^9	9.58×10^9	9.57×10^9	3.06×10^{10}
Diffraction efficiency (photons MGy^{-1})	1.26×10^9	2.45×10^9	1.26×10^9	2.00×10^9	1.26×10^9
Average dose (exposed region) (MGy)	1.12	0.65	3.49	2.41	11.17
Maximum dose (MGy)	23.673	4.387	73.977	21.446	236.725
Dose contrast	9.78	2.65	9.78	3.51	9.78
Used volume, fractional	10.8%	18.4%	10.8%	15.6%	10.8%
Used volume, absolute (μm^3)	61236	104328	61236	88452	104328
DANO peak height #1 (r.m.s.)	13.37	10.64	8.99	11.58	9.41
DANO peak height #2 (r.m.s.)	12.51	10.59	7.96	10.14	8.07

tivity may explain why the HS data are comparable with those from the STD procedure.

3.4. Maltose operon periplasmic protein

MalM (Gilson *et al.*, 1986) crystallizes as well formed, very thin and long needles of uniform thickness (typically 10 μm × 10 μm × 100 μm, Table S1; Fig. S6). The unit cell constants are $a = b = 102.9$ Å, $c = 384.5$ Å, in space group $P4_12_12$ or $P4_32_12$. The crystals are very sensitive to X-rays, diffracting initially to 3.5 Å resolution but decaying rapidly to 7 Å within 7 MGy (10 s) in the X-ray beam. To try to solve the crystal structure, we attempted to collect at a lower X-ray dose rate by attenuating the beam using both HS and STD strategies. Although both attempts failed, the results can be used to compare the performance of the STD and HS methods. The crystal was thin, but long (10 μm × 10 μm × 246 μm; Fig. S6); diffraction data were collected at the Se *K*-edge peak (12.665 keV) in the following order: HS, STD, then another HS at three times the flux. The average dose (8.1–32.9 MGy), average diffraction weighted dose (8.5–42.7 MGy) and maximum dose (19.2–176.7 MGy) for the data collections were all rather high. Furthermore, the *RADDOSE-3D* (Zeldin, Gerstel *et al.*, 2013) calculations suggest that there may have been overlap in the exposed regions between the data sets as the combined volume of the exposed regions is greater than 100%. The diffraction and anomalous signals are clearly better for the HS diffraction data (Fig. S6) as are all of the other data quality indicators. Although to date the structure remains unsolved, as neither the improved HS data nor the STD data have permitted us to locate the selenium atoms and phase the crystal structure, a multi-crystal strategy with HS data collection might eventually succeed.

3.5. Analysis of data scaling

Although any discussion related to the scaling of HS data is beyond the scope of this article, certain general observations regarding the intra-sweep scaling of STD and HS data must be noted. The scaling procedures used by various programmes adopt complex scaling models, from which a scale and *B*-factor can be derived (Kabsch, 2010*b*; Evans & Murshudov, 2013; Otwinowski *et al.*, 2003). Depending on the model used, the *B*-factor also corrects for the resolution dependent crystal decay due to radiation damage. For this reason, only the unscaled I_{mean} plots between HS and STD data collections are compared (Fig. 4). In all cases a drop in the I_{mean} values within the first frames of the data collection is observed. When raw

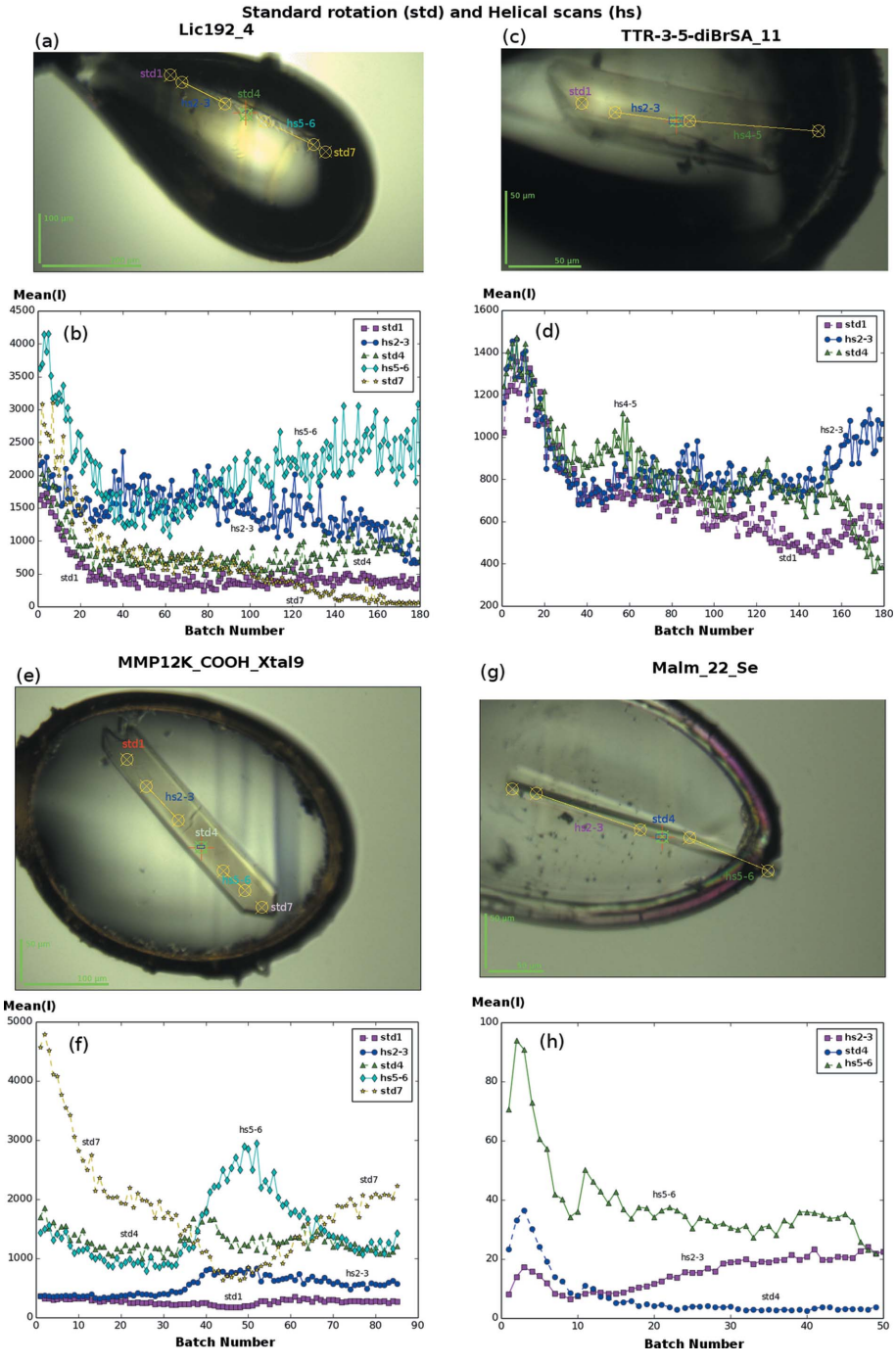

Figure 4
Snapshots and mean raw intensity plots for the cases presented here. (*a*, *b*) Crystal of TTR complexed with a chlorinated ligand. (*c*, *d*) Crystal of TTR bound to a brominated ligand. (*e*, *f*) Crystal of MMP-12. (*g*, *h*) Crystal of MalM.

unscaled intensities from the INTEGRATE step in *XDS* (Kabsch, 2010*b*) were input into *AIMLESS* (Evans & Murshudov, 2013) for the calculation of individual scale and *B*-factors per image, the *B*-factors of the HS data sweeps are always lower in magnitude compared with those for STD data for the cases presented here (Fig. 2). This confirms the observations in the electron density maps, that there is less radiation damage in HS data.

4. Discussion

Radiation damage has been a serious issue in macromolecular crystallography ever since the use of the intense X-ray sources at synchrotrons (Wilson *et al.*, 1983). To limit the adverse effects, structural biologists have developed a variety of methods, such as cryo-cooling (Hope, 1988), the optimization of data collection parameters using dose calculations (Owen *et al.*, 2006; Leal *et al.*, 2011), the use of free radical scavengers (Southworth-Davies & Garman, 2007; Murray & Garman, 2002) and the averaging from multiple crystals (Liu *et al.*, 2012, 2013). PROXIMA 2A is a micro-focus synchrotron beamline and, like similar beamlines, the flux is concentrated into a small area, smaller than the dimensions of a typical crystal (Duran *et al.*, 2013; Smith *et al.*, 2012) causing great local radiation damage. Thus it has become important to develop methods that spread the dose over a wider area. Such methods include collecting multiple wedges at different parts of the crystal, offsetting the rotation axis (Zeldin, Brockhauser *et al.*, 2013) and helical scans (Hilgart *et al.*, 2011; Flot *et al.*, 2010).

In this comparative study between HS and STD data collection strategies, we observe that HS yields the most significant improvements for thin crystals and for those containing X-ray sensitive and labile anomalous scatters, giving better statistics than STD in most cases. For those crystals that are thin, the higher-quality data allow a greater definition of the maps (Fig. 2). The metrics used here to detect radiation damage ($R_{\rm meas}$, $\langle I/\sigma_I\rangle$, $CC_{1/2}$, $CC_{\rm ano}$, $\sigma_{\rm ano}$) have all been thoroughly reviewed (Dauter, 2006; Garman & Nave, 2009; Garman, 2010; Borek *et al.*, 2010). Most of these crystallographic metrics improve with HS; although these improvements may be slight, they translate into better electron density maps showing more detail for thin crystals. The magnitude of improvement, however, is sample dependent.

For crystals containing heavy atoms, the energy absorption by the anomalous scatterers increases the dose rate and thus the damage rate. The bromine phasing example highlights the more significant loss of the anomalous scattering power during STD data collection (Fig. 3; Table 2). The fragility of the

C—Br bond in brominated guanines has been studied and analysed quantitatively by Raman spectroscopy (McGeehan *et al.*, 2007). Such radiation-induced debromination of chemically synthesized brominated nucleic acids poses a serious problem for structure determination using the anomalous scattering effects of bromine. Even at relatively moderate X-ray doses, there is steady and significant debromination during data collection, which destroys its phasing power (Ennifar *et al.*, 2002; Schiltz *et al.*, 2004; Koch *et al.*, 2011), except in some cases of well diffracting crystals, where it can be exploited for RIP phasing (Ravelli *et al.*, 2003).

Selenomethionine is also very sensitive to the exposure of X-rays, where the radiation damage results in the attenuation of the white-line feature in its XANES spectra (Holton, 2007). The rate of decay at the selenium sites depends upon their surrounding environment, and even the chemical composition of the mother liquor solution used for crystallization (Leiros *et al.*, 2006; Holton, 2007). Thus thin crystals containing such a sensitive anomalous scatterer display particularly fast radiation damage, exemplified by MalM crystals, where the initial diffraction limit of 3.5 Å dropped to below 6 Å within five frames (Table S1; Fig S6). Although the use of HS helped extend the overall resolution limit, this was not sufficient to collect enough anomalous data to solve the selenium substructure.

In contrast, the stability of the zinc ions in the MMP-12 example (Fig. S4), along with the much thicker dimensions of the crystal compared with the X-ray beam focus, translates into similar MX quality metrics between STD and HS data sets (Table 3). Zinc ions are bound tightly by their protein ligands, resist reduction and oxidation, so that they retain their position and do not diffuse away. Chemical stability ensures that the anomalous data are preserved over larger doses. However, X-rays are known to induce changes at activated ligands, which are bound to Zn^{2+} sites in zinc metallo-enzymes, such as human carbonic anhydrase (Sjöblom *et al.*, 2009).

In SAD data collections, the need for high multiplicity often conflicts with radiation damage effects (Liu *et al.*, 2012, 2013). Higher multiplicity increases the accuracy of weak anomalous signals, as long as this signal is not contaminated by the manifestations of radiation damage that increase with higher doses. Indeed, for phasing experiments such as sulfur SAD, which require multiplicities typically above 50, the crystals must be particularly resistant (Dauter *et al.*, 2002). HS data collection methods have an advantage, because the dose is distributed over a larger volume, which permits for a greater multiplicity, and also it avoids excessive radiation-damage-induced non-isomorphism, if the crystal is susceptible to lattice expansion under intense X-rays (Ravelli & McSweeney, 2000). Thus, HS data collections are suitable for delicate samples and for SAD phasing where long crystals are available.

Since HS methods are different between data collections in 'shuttered' and 'shutterless' modes, this study will need to be repeated in the 'shutterless' mode. The results presented here were carried out with an ADSC Q315r, which functions in 'shuttered' mode with a dwell time of approximatively 2 s between images. Fortunately, the area detector on PROXIMA 2A has been upgraded to an EIGER X 9M (Dectris), which functions in 'shutterless' mode. Now the sample moves continuously during exposure to X-rays in HS data collections, while previously, in 'shuttered' mode, the crystal was stationary during the acquisition of each image and then moved to the next position when the shutter was closed. With the beamline fully upgraded, on the basis of this prior study, a new HS strategy can be put in place.

5. Conclusion

The improvements from the use of helical scans is reflected in the quality of the X-ray diffraction data and often yields better detail in the final electron density maps. The differences upon visual inspection of STD and HS maps, imperceptible at first glance, become evident during the interpretation of the electron density. Even minor improvements can become significant in the context of drug discovery and design, where the evaluation of a lead compound depends upon the clarity of its presence and orientation. HS methods can also make a difference when trying to solve a structure *via* SAD methods by preserving the signal of sensitive and labile anomalously scattering atoms. The type of anomalous scatterer and its redox chemistry should be carefully considered before collecting data, as certain anomalous scattering atoms are more sensitive to X-rays than others (Br *versus* Zn^{2+}).

Overall, HS data give better maps since the dose of the X-rays is distributed over a larger volume of the sample, leading to less radiation damage and greater chemical integrity. The advantages are clearly illustrated by the improvement in the detail of the electron density maps and in the conservation of C—Br bonds of brominated ligands, such as drug compounds and nucleotides (Ennifar *et al.*, 2002). In fact, the sensitivity of C—Br bonds to X-rays can be exploited as an internal measure of radiation damage.

However, the macroscopic structure of the crystalline sample must be homogeneous for HS methods to give this advantage. The presence of cracks, dislocations, unit cell variations or any other inhomogeneities, which would degrade the X-ray diffraction pattern, will consequently be reflected in the indexing, integration and scaling of the data processing.

PROXIMA 2A has characteristics similar to those of many other micro-focused beamlines, so that the HS methods used here should be easily employed at other sites and our analysis, attempts and guidelines could be optimized for use at other installations. In time, the advantages of this technique might become appreciated even by those crystallographers who currently are suspicious of the method.

Acknowledgements

We wish to thank Dr Ahmed Haouz of the Crystallization Platform (PF6) at the Pasteur Institute in Paris, France, for the generous donation of MalM crystals, and the staff of the PROXIMA 2A at Synchrotron SOLEIL for technical assistance. We acknowledge funding from the ERASMUS program (IP).

References

Adams, P. D., Afonine, P. V., Bunkóczi, G., Chen, V. B., Davis, I. W., Echols, N., Headd, J. J., Hung, L.-W., Kapral, G. J., Grosse-Kunstleve, R. W., McCoy, A. J., Moriarty, N. W., Oeffner, R., Read, R. J., Richardson, D. C., Richardson, J. S., Terwilliger, T. C. & Zwart, P. H. (2010). *Acta Cryst.* D**66**, 213–221.

Alkire, R. W., Rosenbaum, G. & Evans, G. (2000). *J. Synchrotron Rad.* **7**, 61–68.

Alkire, R. W., Rotella, F. J. & Duke, N. E. C. (2013). *J. Appl. Cryst.* **46**, 525–536.

Borek, D., Cymborowski, M., Machius, M., Minor, W. & Otwinowski, Z. (2010). *Acta Cryst.* D**66**, 426–436.

Bourenkov, G. P. & Popov, A. N. (2010). *Acta Cryst.* D**66**, 409–419.

Bowler, M. G. & Bowler, M. W. (2014). *Acta Cryst.* F**70**, 127–132.

Bowler, M. W., Guijarro, M., Petitdemange, S., Baker, I., Svensson, O., Burghammer, M., Mueller-Dieckmann, C., Gordon, E. J., Flot, D., McSweeney, S. M. & Leonard, G. A. (2010). *Acta Cryst.* D**66**, 855–864.

Burmeister, W. P. (2000). *Acta Cryst.* D**56**, 328–341.

Ciccone, L., Tepshi, L., Nencetti, S. & Stura, E. A. (2015). *New Biotechnol.* **32**, 54–64.

Dauter, Z. (2006). *Acta Cryst.* D**62**, 867–876.

Dauter, Z., Dauter, M. & Dodson, E. J. (2002). *Acta Cryst.* D**58**, 494–506.

Duran, D., Le Couster, S., Desjardins, K., Delmotte, A., Fox, G., Meijers, R., Moreno, T., Savko, M. & Shepard, W. (2013). *J. Phys. Conf. Ser.* **425**, 012005.

Emsley, P., Lohkamp, B., Scott, W. G. & Cowtan, K. (2010). *Acta Cryst.* D**66**, 486–501.

Ennifar, E., Carpentier, P., Ferrer, J.-L., Walter, P. & Dumas, P. (2002). *Acta Cryst.* D**58**, 1262–1268.

Evans, P. R. & Murshudov, G. N. (2013). *Acta Cryst.* D**69**, 1204–1214.

Flot, D., Mairs, T., Giraud, T., Guijarro, M., Lesourd, M., Rey, V., van Brussel, D., Morawe, C., Borel, C., Hignette, O., Chavanne, J., Nurizzo, D., McSweeney, S. & Mitchell, E. (2010). *J. Synchrotron Rad.* **17**, 107–118.

Gabadinho, J., Beteva, A., Guijarro, M., Rey-Bakaikoa, V., Spruce, D., Bowler, M. W., Brockhauser, S., Flot, D., Gordon, E. J., Hall, D. R., Lavault, B., McCarthy, A. A., McCarthy, J., Mitchell, E., Monaco, S., Mueller-Dieckmann, C., Nurizzo, D., Ravelli, R. B. G., Thibault, X., Walsh, M. A., Leonard, G. A. & McSweeney, S. M. (2010). *J. Synchrotron Rad.* **17**, 700–707.

Garman, E. F. (2010). *Acta Cryst.* D**66**, 339–351.

Garman, E. F. & Nave, C. (2009). *J. Synchrotron Rad.* **16**, 129–132.

Gerstel, M., Deane, C. M. & Garman, E. F. (2015). *J. Synchrotron Rad.* **22**, 201–212.

Gilson, E., Rousset, J., Charbit, A., Perrin, D. & Hofnung, M. (1986). *J. Mol. Biol.* **191**, 303–311.

Hilgart, M. C., Sanishvili, R., Ogata, C. M., Becker, M., Venugopalan, N., Stepanov, S., Makarov, O., Smith, J. L. & Fischetti, R. F. (2011). *J. Synchrotron Rad.* **18**, 717–722.

Holton, J. M. (2007). *J. Synchrotron Rad.* **14**, 51–72.

Hope, H. (1988). *Acta Cryst.* B**44**, 22–26.

Incardona, M.-F., Bourenkov, G. P., Levik, K., Pieritz, R. A., Popov, A. N. & Svensson, O. (2009). *J. Synchrotron Rad.* **16**, 872–879.

Johnson, S. M., Connelly, S., Wilson, I. A. & Kelly, J. W. (2009). *J. Med. Chem.* **52**, 1115–1125.

Kabsch, W. (2010*a*). *Acta Cryst.* D**66**, 125–132.

Kabsch, W. (2010*b*). *Acta Cryst.* D**66**, 133–144.

Koch, C., Heine, A. & Klebe, G. (2011). *J. Synchrotron Rad.* **18**, 782–789.

Leal, R. M. F., Bourenkov, G. P., Svensson, O., Spruce, D., Guijarro, M. & Popov, A. N. (2011). *J. Synchrotron Rad.* **18**, 381–386.

Leiros, H.-K. S., Timmins, J., Ravelli, R. B. G. & McSweeney, S. M. (2006). *Acta Cryst.* D**62**, 125–132.

Liu, Q., Dahmane, T., Zhang, Z., Assur, Z., Brasch, J., Shapiro, L., Mancia, F. & Hendrickson, W. A. (2012). *Science*, **336**, 1033–1037.

Liu, Q., Liu, Q. & Hendrickson, W. A. (2013). *Acta Cryst.* D**69**, 1314–1332.

McGeehan, J. E., Carpentier, P., Royant, A., Bourgeois, D. & Ravelli, R. B. G. (2007). *J. Synchrotron Rad.* **14**, 99–108.

Meerts, I. A., van Zanden, J. J., Luijks, E. A., van Leeuwen-Bol, I., Marsh, G., Jakobsson, E., Bergman, A. & Brouwer, A. (2000). *Toxicol. Sci.* **56**, 95–104.

Morse, J., Salomé, M., Berdermann, E., Pomorski, M., Cunningham, W. & Grant, J. (2007). *Diamond Relat. Mater.* **16**, 1049–1052.

Murray, J. & Garman, E. (2002). *J. Synchrotron Rad.* **9**, 347–354.

Murshudov, G. N., Skubák, P., Lebedev, A. A., Pannu, N. S., Steiner, R. A., Nicholls, R. A., Winn, M. D., Long, F. & Vagin, A. A. (2011). *Acta Cryst.* D**67**, 355–367.

Otwinowski, Z., Borek, D., Majewski, W. & Minor, W. (2003). *Acta Cryst.* A**59**, 228–234.

Owen, R. L., Rudino-Pinera, E. & Garman, E. F. (2006). *Proc. Natl Acad. Sci. USA*, **103**, 4912–4917.

Pape, T. & Schneider, T. R. (2004). *J. Appl. Cryst.* **37**, 843–844.

Pozharski, E. (2012). *Acta Cryst.* D**68**, 1077–1087.

Ravelli, R. B. G., Leiros, H. S. K. S., Pan, B., Caffrey, M. & McSweeney, S. (2003). *Structure*, **11**, 217–224.

Ravelli, R. B. & McSweeney, S. M. (2000). *Structure*, **8**, 315–328.

Schiltz, M., Dumas, P., Ennifar, E., Flensburg, C., Paciorek, W., Vonrhein, C. & Bricogne, G. (2004). *Acta Cryst.* D**60**, 1024–1031.

Schneider, T. R. & Sheldrick, G. M. (2002). *Acta Cryst.* D**58**, 1772–1779.

Shayduk, R. & Braun, W. (2008). *J. Appl. Cryst.* **41**, 768–775.

Sheldrick, G. M. (2002). *Z. Kristallogr.* **217**, 644–650.

Sheldrick, G. M. (2008). *Acta Cryst.* A**64**, 112–122.

Sjöblom, B., Polentarutti, M. & Djinovic Carugo, K. (2009). *Proc. Natl Acad. Sci. USA*, **106**, 10609–10613.

Smith, J. L., Fischetti, R. F. & Yamamoto, M. (2012). *Curr. Opin. Struct. Biol.* **22**, 602–612.

Song, J., Mathew, D., Jacob, S. A., Corbett, L., Moorhead, P. & Soltis, S. M. (2007). *J. Synchrotron Rad.* **14**, 191–195.

Southworth-Davies, R. J. & Garman, E. F. (2007). *J. Synchrotron Rad.* **14**, 73–83.

Terwilliger, T. C., Grosse-Kunstleve, R. W., Afonine, P. V., Moriarty, N. W., Zwart, P. H., Hung, L.-W., Read, R. J. & Adams, P. D. (2008). *Acta Cryst.* D**64**, 61–69.

Vagin, A. & Teplyakov, A. (2010). *Acta Cryst.* D**66**, 22–25.

Vera, L., Antoni, C., Devel, L., Czarny, B., Cassar-Lajeunesse, E., Rossello, A., Dive, V. & Stura, E. A. (2013). *Cryst. Growth Des.* **13**, 1878–1888.

Weik, M., Bergès, J., Raves, M. L., Gros, P., McSweeney, S., Silman, I., Sussman, J. L., Houée-Levin, C. & Ravelli, R. B. G. (2002). *J. Synchrotron Rad.* **9**, 342–346.

Weik, M., Ravelli, R. B. G., Kryger, G., McSweeney, S., Raves, M. L., Harel, M., Gros, P., Silman, I., Kroon, J. & Sussman, J. L. (2000). *Proc. Natl Acad. Sci. USA*, **97**, 623–628.

Wilson, K. S., Stura, E. A., Wild, D. L., Todd, R. J., Stuart, D. I., Babu, Y. S., Jenkins, J. A., Standing, T. S., Johnson, L. N., Fourme, R., Kahn, R., Gadet, A., Bartels, K. S. & Bartunik, H. D. (1983). *J. Appl. Cryst.* **16**, 28–41.

Winn, M. D., Ballard, C. C., Cowtan, K. D., Dodson, E. J., Emsley, P., Evans, P. R., Keegan, R. M., Krissinel, E. B., Leslie, A. G. W., McCoy, A., McNicholas, S. J., Murshudov, G. N., Pannu, N. S., Potterton, E. A., Powell, H. R., Read, R. J., Vagin, A. & Wilson, K. S. (2011). *Acta Cryst.* D**67**, 235–242.

Zeldin, O. B., Brockhauser, S., Bremridge, J., Holton, J. M. & Garman, E. F. (2013). *Proc. Natl Acad. Sci. USA*, **110**, 20551–20556.

Zeldin, O. B., Gerstel, M. & Garman, E. F. (2013). *J. Appl. Cryst.* **46**, 1225–1230.